Geophysical Prospecting, 2008, **56**, 375–393 doi:10.1111/j.1365-2478.2007.00684.x

Cross-correlation of random fields: mathematical approach and applications

P. Gouédard[1*], L. Stehly[1,2], F. Brenguier[1,3], M. Campillo[1], Y. Colin de Verdière[4], E. Larose[1], L. Margerin[5], P. Roux[1], F. J. Sánchez-Sesma[6], N. M. Shapiro[3] and R. L. Weaver[7]

[1]*Laboratoire de Géophysique Interne et de Tectonophysique, Observatoire de Grenoble, Université Joseph Fourier, Grenoble, France,* [2]*CEA/DASE, Bruyères-le-Châtel, France,* [3]*Laboratoire de Sismologie, Institut de Physique du Globe de Paris, CNRS, Paris, France,* [4]*Institut Fourier, Université Joseph Fourier, Grenoble, France,* [5]*CEREGE, Europôle Méditerranéen de l'Arbois, Aix-en-Provence, France,* [6]*Instituto de Ingeniería, Universidad Nacional Autónoma de México, Coyoacán, Mexico, and* [7]*Department of Physics, University of Illinois, Urbana, Illinois, USA*

Received February 2007, revision accepted October 2007

ABSTRACT

Random field cross-correlation is a new promising technique for seismic exploration, as it bypasses shortcomings of usual active methods. Seismic noise can be considered as a reproducible, stationary in time, natural source. In the present paper we show why and how cross-correlation of noise records can be used for geophysical imaging. We discuss the theoretical conditions required to observe the emergence of the Green's functions between two receivers from the cross-correlation of noise records. We present examples of seismic imaging using reconstructed surface waves from regional to local scales. We also show an application using body waves extracted from records of a small-scale network. We then introduce a new way to achieve surface wave seismic experiments using cross-correlation of unsynchronized sources. At a laboratory scale, we demonstrate that body wave extraction may also be used to image buried scatterers. These works show the feasibility of passive imaging from noise cross-correlation at different scales.

INTRODUCTION

Traditional observational methods in seismology are based on earthquake records which results in two main shortcomings:

1 Most techniques are based on waves emitted by earthquakes that occurred only in geologically active areas, mainly plate boundaries. This results in a limited resolution in all other areas where earthquakes are not present. In particular, at stations far away from the source region, all the high-frequency information is lost due to the attenuation of the medium.

2 The occurrence of earthquakes is too low, preventing the study of real time change of active structures such as volcanoes or faults.

In the case of active seismic at smaller scales, the resolution is limited by the number and power of sources. It is thus difficult to image large areas or deep structures. Furthermore, controlled sources are difficult to carry out on hardly accessible places, like at the ocean bottom, where passive imaging could be much more convenient. For time-lapse monitoring, reproducible sources are necessary. This is very difficult to achieve for surveys of long duration, whereas noise wavefields may be stationary on these time scales.

Here we explore an alternative way of probing the Earth's interior using noise records only. The main idea is to consider seismic noise as a random source field when averaged over a long time series. In this particular case, cross-correlation between two stations yields the Green's function between these two points. As the seismic noise is mainly generated by atmospheric and oceanic forcing at the Earth's surface, the surface

*E-mail: pierre.gouedard@ujf-grenoble.fr

wave part of the Green's function is mostly extracted from the cross-correlation process.

At smaller scales, the same principle can be applied to study local structures. In this case, higher frequencies are used. At these frequencies, the wavefield is believed to be governed by local sources, which are unlikely to have the expected properties of randomness. This has to be taken into account in the processing.

In this paper, the theoretical relationship between noise cross-correlation and the Green's function is first discussed in section 2, based on theoretical derivations from (Colin de Verdière 2006a,b). Several applications are then presented, from large to small scales, using noise wavefields of different origin and physical properties: surface wave tomography at the regional scale in Western Europe (section 3) and at a more local scale in section 4 at the 'Piton de la Fournaise' volcano (Brenguier *et al.* 2007); local P-waves extraction in the Parkfield network at the San Andreas Fault (Roux *et al.* 2005a) in section 5; site characterization using surface waves extracted from noise cross-correlation (Gouédard *et al.* 2006) in section 6; passive imaging of a buried scatterer at laboratory scale (Larose *et al.* 2006b) in section 7.

BACKGROUND AND MATHEMATICAL APPROACH

Historical background

The Green's function of a medium between two points A and B represents the record we would obtain at A if an impulsive source is applied at B.

In the case of a completely random wavefield, the cross-correlation of signals recorded between two points converges to the complete Green's function of the medium, including all reflection, scattering and propagation modes (Weaver 2005). To demonstrate this result and to define more precisely under which assumption it is valid, various experimental, numerical and theoretical approaches have been developed.

Historically speaking, helioseismology was the first field where ambient-noise cross-correlation performed from recordings of the Sun's surface random motion was used to retrieve time-distance information on the solar surface (Duvall *et al.* 1993; Gilles *et al.* 1997). The idea of day-light imaging was proposed by Claerbout (1968) in the context of prospecting. More recently, a seminal paper was published by Weaver and Lobkis (2001) that showed how diffuse thermal noise recorded and cross-correlated at two transducers fastened to one face of an aluminium sample provided the complete Green's function between these two points. They theoretically interpreted this result by invoking equipartitioning of the modes excited in the aluminium sample. This result was generalized to the case where randomization is not produced by the distribution of sources, but is provided by multiple scattering that takes place in heterogeneous media (Lobkis and Weaver 2001).

The use of a spectral representation (Lobkis and Weaver 2001), the fluctuation-dissipation approach (Weaver and Lobkis 2001, 2003; van Tiggelen 2003; Godin 2007) or a correlation-type representation theorem (e.g. Wapenaar 2004) are rigorous theoretical approaches to interpret experimental results.

Experimental evidences demonstrated the feasibility of passive imaging in 1) acoustics (Lobkis and Weaver 2001; Weaver and Lobkis 2001; Larose *et al.* 2004), 2) seismology where Campillo and Paul (2003) retrieve the Green's function between two seismic stations from a collection of earthquakes, and 3) oceanography in shallow underwater acoustics where both direct and reflected wavefronts were retrieved from ambient-noise cross-correlation (Roux and Kuperman 2004; Sabra *et al.* 2005b). By summing the contributions of all sources to the correlation, it has been shown numerically that the correlation contains the causal and acausal Green's function of the medium (Wapenaar 2004). Cases of non-reciprocal (e.g. in the presence of a flow) or inelastic media have also been theoretically investigated (Wapenaar 2006; Godin 2007).

Derode *et al.* (2003a,b) proposed to interpret the Green's function reconstruction in terms of a time-reversal analogy and showed that correlation of multiply scattered waves could be used for passive imaging in acoustics. The convergence of the noise correlation function towards the Green's function in an unbounded medium can also be interpreted through the stationary phase theorem (Snieder 2004; Roux *et al.* 2005b).

In seismology, Aki (1957) proposed a long time ago to use seismic noise to retrieve the dispersion properties of surface waves in the subsoil. Shapiro and Campill (2004) reconstructed the surface wave part of the Green's function by correlating seismic noise at stations separated by distances of hundreds to thousands of kilometres, and measured their dispersion curves at periods ranging from 5 to about 150 seconds. This method led to the first application of passive seismic imaging in California (Shapiro *et al.* 2005; Sabra *et al.* 2005a) with a much greater spatial accuracy than for usual active techniques. Larose *et al.* (2005) also used noise cross-correlation at small distances on the moon.

For the problem of elastic waves, it has been theoretically shown that the convergence of noise correlation to the

Green's function was bonded by the equipartition condition of the different components of the elastic field (Sánchez-Sesma *et al.* 2006a, 2007). In other words, the emergence of the Green's function is effective after a sufficient self-averaging process that is provided by random spatial distribution of the noise sources when considering long time series as well as scattering (Campillo 2006; Larose *et al.* 2006a).

The case of homogeneously distributed white noise sources

The scope of this section is to summarize the different theoretical approaches using mathematical tools that allow a global view of the correlation problem in any propagation medium. We will see that cross-correlation of noise recorded at two distant stations A and B yields the Green's function, assuming that the wavefield is a white noise distributed everywhere in the medium, with no assumption about the medium.

We consider any medium X, that does not need to be homogeneous, where the wave propagation equation is controlled by a damped equation that can be written as:

$$\frac{\partial^2 u}{\partial t^2} + 2\,a\,\frac{\partial u}{\partial t} - L\,u = f \tag{1}$$

Here $a > 0$ is a constant that corresponds to the attenuation of the medium, $f(t, \vec{r})$ is the source field (i.e. the noise field in our case) and $u(t, \vec{r})$ denotes the displacement field. If $L = c^2(\vec{r})\,\Delta$, we recognize the usual wave equation. In a more general calculation, L can be any negative self-adjoint elliptic differential operator. In more physical terms, L is an operator which preserves energy.

First of all we will introduce a definition of the Green's function in the frequency domain using the *integral kernel* of the operator L, and show that this definition is equivalent to the usual one. Then, by expressing the displacement field using the Green's function, we will calculate the cross-correlation and find how the derivative of the cross-correlation function is linked to the Green's function.

We introduce the integral kernel of an operator P, denoted by $[\![P]\!](x, y)$ by:

$$\forall u : X \longmapsto \mathbb{R}^3,\ (Pu)(x) = \int_X [\![P]\!](x, y)\, u(y)\, dy$$

This is the 'continuous matrix' of the operator P. It has to be linked to the case of a finite space where one can define the matrix (P_{ij}) of P and write the following formula:

$$\forall u : X \longmapsto \mathbb{R}^3,\ (Pu)_i = \sum_j P_{ij}\, u_j$$

We first consider a medium without attenuation, i.e. $a = 0$ in equation 1. Let us define the Green's function of L in the frequency domain, denoted by $\hat{G}(\omega + i\,\varepsilon, \vec{r}, \vec{r}_s)$, with ε a small positive value, as the opposite of the integral kernel of $((\omega + i\,\varepsilon)^2 + L)^{-1}$. In other words, $\hat{G}$ is the *resolvent* of L evaluated at point $(\omega + i\,\varepsilon)^2$. The $\hat{}$ denotes a function defined in the Fourier space. ε ensures that $((\omega + i\,\varepsilon)^2 + L)$ is invertible as L has real eigenvalues. We will show that this mathematical definition of $\hat{G}$ is the same as the usual one, which is the causal solution of the wave equation (equation 1) when the source function f is a Dirac impulse in time and space $\delta(t, \vec{r} - \vec{r}_s)$. The Green's function $\hat{G}(\omega + i\,\varepsilon, \vec{r}, \vec{r}_s)$ admits a limit as $\varepsilon \to 0^+$, denoted by $\hat{G}(\omega + i0, \vec{r}, \vec{r}_s)$, as a Schwartz distribution on the real axis. If L has a continuous spectrum, this limit is a smooth function (the 'limiting absorption principle'). $\hat{G}$ can thus be written as:

$$\begin{aligned}
\hat{G}(\omega + i0, \vec{r}, \vec{r}_s) &= -[\![((\omega + i0)^2 + L)^{-1}]\!](\vec{r}, \vec{r}_s)\\
&= -\int_X [\![((\omega + i0)^2 + L)^{-1}]\!]\\
&\qquad \times (\vec{r}, \vec{r}\,')\, \delta(\vec{r}\,' - \vec{r}_s)\, d\vec{r}\,'\\
&= -((\omega + i0)^2 + L)^{-1}\, \delta(\vec{r} - \vec{r}_s)
\end{aligned}$$

which yields:

$$-((\omega + i0)^2 + L)\, \hat{G}(\omega + i0, \vec{r}, \vec{r}_s) = \delta(\vec{r} - \vec{r}_s)$$

The inverse Fourier transform of this equation gives a relation that is the usual definition of G in the case of a medium without attenuation:

$$\frac{\partial^2 G}{\partial t^2}(t, \vec{r}, \vec{r}_s) - L\, G(t, \vec{r}, \vec{r}_s) = \delta(t)\, \delta(\vec{r} - \vec{r}_s)$$

G is thus the solution of equation 1 in the case of an impulsive source in time and space. One can compute the inverse Fourier transform of $\hat{G}(\omega + i\varepsilon, x, y)$ using residue calculus, and take the limit as ε goes to 0 to obtain

$$G(t, \vec{r}, \vec{r}_s) = Y(t) \left[\!\!\left[\frac{\sin t\sqrt{-L}}{\sqrt{-L}} \right]\!\!\right] (\vec{r}, \vec{r}_s)$$

where Y is the Heaviside-step function, and where we denote $\sqrt{-L}$ the operator which eigenvalues are the images of the eigenvalues of L by the function $x \mapsto \sqrt{-x}$ (idem for the sinus function).

If we consider an attenuating medium, the Green's function $\hat{G}_a(\omega, \vec{r}, \vec{r}_s)$ is defined by the resolvent of L evaluated at point $\omega^2 + 2\,i\,a\,\omega$ instead of $(\omega + i0)^2$. It thus becomes

$$G_a(t, \vec{r}, \vec{r}_s) = Y(t)\, e^{-a\,t} \left[\!\!\left[\frac{\sin t\sqrt{-L - a^2}}{\sqrt{-L - a^2}} \right]\!\!\right] (\vec{r}, \vec{r}_s) \tag{2}$$

We now define the time domain cross-correlation between the displacement at two points A and B as:

$$C(\tau, \vec{r}_A, \vec{r}_B) = \lim_{T\to+\infty} \frac{1}{T} \int_0^T u(t, \vec{r}_A)\, \overline{u(t+\tau, \vec{r}_B)}\, dt \tag{3}$$

where the bar denotes the conjugate. $u(t, \vec{r})$ can be expressed using the Green's function G_a (here attenuation is necessary to ensure convergence of the integral, see Roux *et al.* (2005b)) and the source function f as follows:

$$u(t, \vec{r}) = \int_0^\infty dt' \int_X G_a(t', \vec{r}, \vec{r}_s)\, f(t - t', \vec{r}_s)\, d\vec{r}_s$$

We assume that f is a white noise distributed everywhere in the medium X, acting at any time t. In the frequency domain, a white noise contains all the frequencies with a random phase. In the time domain, this is a random wavefield such that the position and the activation time of each source are uncorrelated. In this case, and considering a damping medium, we replace the large T limit in the correlation by an ensemble average. We then obtain the following explicit expression for the correlation between the wavefields recorded at A and B (see Appendix A for mathematical details):

$$C(\tau, \vec{r}_A, \vec{r}_B) = \frac{\sigma^2\, e^{-a|\tau|}}{4a} \left[\!\left[(-L)^{-1} \left(\cos \tau\sqrt{-L-a^2} + a\, \frac{\sin|\tau|\sqrt{-L-a^2}}{\sqrt{-L-a^2}} \right) \right]\!\right] (\vec{r}_A, \vec{r}_B) \tag{4}$$

where σ is the variance of the noise wavefield.

The time derivative of this equation is expressed in terms of the Green's function using (2), giving the more familiar expression:

$$\frac{d}{d\tau} C(\tau, \vec{r}_A, \vec{r}_B) = \frac{-\sigma^2}{4a} (G_a(\tau, \vec{r}_A, \vec{r}_B) - G_a(-\tau, \vec{r}_A, \vec{r}_B)) \tag{5}$$

This means that for any medium, the time-derivative of the cross-correlation computed between the wavefields recorded at two stations A and B is the Green's function of the medium, provided that the damping coefficient is small enough and that noise sources behave as white noise acting everywhere in the medium. This is the same hypothesis as stated in Roux *et al.* (2005b), Lobkis and Weaver (2001) and others, but L is now an arbitrary negative definite elliptic operator, and so the present result is more general.

The case of a scattering medium

The previous calculation was made using sources randomly located anywhere and randomly active at any time. This is a very strong hypothesis that is not valid in practical cases. Another demonstration of the link between cross-correlations and Green's functions can be made without any assumption about the noise sources location or their activation time. We only assume that there is equipartition at the boundaries of the region of interest, which means that each eigenmode is excited with the same level of energy.

A simple view of the relation between equipartition and correlation is given by the reconstruction of the Green's function of the homogeneous space using the azimuthal averaging of the correlation of plane waves, which are the eigenfunctions of the problem. Sánchez-Sesma and Campillo (2006) consider an isotropic distribution of P and S plane waves in an elastic medium. They found that the azimuthal average of the cross-correlation of motion between two points is proportional to the imaginary part of the exact Green's tensor between these points under the condition that the energy ratio S/P of the incident waves is the one predicted by equipartition. These results clearly show that equipartition is a necessary condition to retrieve the exact Green's function from correlations of the elastic field. In practice, one has to deal with complex media for which the eigenfunctions are unknown and therefore for which equipartition conditions cannot be explicitly specified in terms of local properties of the field.

Sánchez-Sesma *et al.* (2006a) discussed a particular case. They considered the field in the vicinity of a cylindrical scatterer embedded in an homogeneous space and illuminated isotropically with incident P and S plane waves in the ratio of equipartition of the homogeneous space. Taking into account the scattered waves, they showed that the azimuthal average of cross-correlations of motion between two points still yields the imaginary part of the exact Green's tensor of the heterogeneous medium, including the scattered waves, even at close distance from the scatterer. Is such a property still valid for any scattered or type of heterogeneity? What are the conditions required for the incident field? Weaver and Lobkis (2004) used an integral representation approach to study the problem of an heterogeneous region in an open medium. The essence of this property is expressed in the spectral theory of scattering that shows that the properties obtained in the simplest case of a homogeneous medium are formally valid in presence of heterogeneities. This is discussed in Colin de Verdière (2006a,b) as follows.

In the first step we will define the *spectral projector* and exhibit its expression using the cross-correlation function (equation 7). In a second step, will prove the relation between this projector and the Green's function, the so-called Stone formula (equation 8).

We denote $e_0(\vec{r}, \vec{k}) = e^{i\,\vec{k}\cdot\vec{r}}$ as the plane waves that are the eigenmodes of the homogeneous infinite space. In the case of a complex medium, the scattering theory (Ramm 1986; Reed and Simon 1978) tells us that, if the medium is heterogeneous only in a finite region, the eigenmodes in the whole space can be written as:

$$e(\vec{r}, \vec{k}) = e_0(\vec{r}, \vec{k}) + e_s(\vec{r}, \vec{k})$$

where e_s, the scattered waves, satisfies the so-called *Sommerfeld radiation* condition, which ensures that e_s will vanish when $\vec{r}$ goes to infinity. This decomposition is still valid in the near field of the scatterers (i.e. inside the heterogeneous region).

For $I \subset \mathbb{R}_+$, we define the spectral projector of L on I, denoted by P_I, from its integral kernel $[\![P_I]\!]$ at any points $\vec{r}_1$ and $\vec{r}_2$ of X by:

$$[\![P_I]\!](\vec{r}_1, \vec{r}_2) = (2\,\pi)^{-d} \int_{\lambda_k \in I} e(\vec{r}_1, \vec{k})\, \overline{e(\vec{r}_2, \vec{k})}\, |d^d\vec{k}| \tag{6}$$

where d is the dimension of the space and λ_k denotes the eigenvalue associated with the eigenfunction $e(\vec{r}, \vec{k})$. This is the projector on the sub-eigenspaces of L which eigenvalues are in I. Again, what P_I represents can be easily understood in the case of a finite number N of eigenvalues $\{\lambda_n\}$, where we can write:

$$[\![P_I]\!](\vec{r}_1, \vec{r}_2) = \sum_{\substack{n\in[1,N]\\ \lambda_n \in I}} e_i(\vec{r}_1)\, \overline{e_n(\vec{r}_2)}$$

In this case, I represents a subset of values of $n \in [1, N]$ that are preserved, all the other being removed by the projector P_I. For example, if $u(\vec{r}) = \sum_{n=1}^{N} u_n\, e_n(\vec{r})$, we have:

$$(P_I\, u)(\vec{r}) = \sum_{\substack{n\in[1,N]\\ \lambda_n \in I}} u_n\, e_n(\vec{r})$$

We now will demonstrate that the derivative of the spectral projector on an interval around a value $\omega^2 \in \mathbb{R}_+$ is linked to the cross-correlation function at the corresponding pulsation ω. We thus consider an interval $I = [\omega_-^2, \omega_+^2]$ around ω^2. The integral over $\lambda_k = c^2\,|\vec{k}|^2 \in I$ in equation 6 defines a volume of integration of dimension d that can be decomposed into two integrals, one over a volume of dimension $d - 1$ defined by $c^2\,|\vec{k}|^2 = \omega^2$ and the other over $|\vec{k}|$:

$$[\![P_I]\!](\vec{r}_1, \vec{r}_2) = (2\,\pi)^{-d} \times \int_{c^2|\vec{k}|^2\in I} \int_{c^2|\vec{k}|^2=\omega^2} e(\vec{r}_1, \vec{k})\, \overline{e(\vec{r}_2, \vec{k})}\, |d^{d-1}\sigma|\, |\vec{k}|^{d-1}\, d|\vec{k}|$$

where $|d^{d-1}\sigma|$ is the usual measure of the unit $(d-1)$–dimensional sphere. In the case $d = 3, d^2\sigma$ is the infinitesimal solid angle. Taking the derivative with respect to ω_+ in this equation gives:

$$\frac{d}{d\omega_+}[\![P_I]\!](\vec{r}_1, \vec{r}_2) = \frac{(2\,\pi)^{-d}}{c}\left(\frac{\omega}{c}\right)^{d-1} \times \int_{c^2|\vec{k}|^2=\omega^2} e(\vec{r}_1, \vec{k})\, \overline{e(\vec{r}_2, \vec{k})}\, |d^{d-1}\sigma|$$

In this formula, one can recognize the cross-correlation of random scattered waves of frequency ω recorded at points $\vec{r}_1$ and $\vec{r}_2$ that can be written as:

$$\hat{C}(\omega, \vec{r}_1, \vec{r}_2) = \frac{1}{\sigma_{d-1}} \int_{c^2|\vec{k}|^2=\omega^2} e(\vec{r}_1, \vec{k})\, \overline{e(\vec{r}_2, \vec{k})}\, |d\sigma|$$

where σ_{d-1} denotes the total volume of the unit sphere in $\mathbb{R}^{d-1}$: $\sigma_0 = 2, \sigma_1 = 2\,\pi, \sigma_2 = 4\,\pi, \ldots$

Using the two previous equations, we find

$$\frac{d}{d\omega}[\![P_I]\!](\vec{r}_1, \vec{r}_2) = \frac{\sigma_{d-1}}{(2\,\pi)^d}\,\frac{1}{c}\left(\frac{\omega}{c}\right)^{d-1} C_\omega(\vec{r}_1, \vec{r}_2) \tag{7}$$

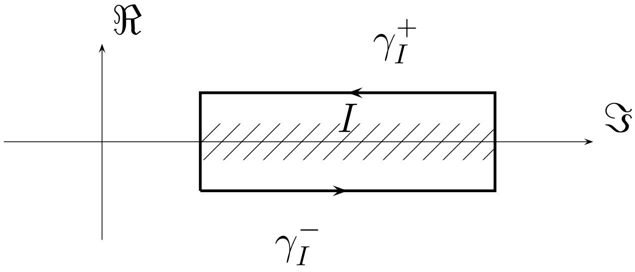

Figure 1 γ_I can be split into two contours γ_I^+ and γ_I^- which are complex conjugate and followed in opposite direction.

The projector P_I defined previously can also be written using the resolvent of the operator L using the Cauchy formula:

$$P_I = \frac{1}{2\,i\,\pi} \int_{\gamma_I} (L + \lambda)^{-1}\, d\lambda$$

where a γ_I is a contour in the complex plane which restriction to the real axis is I. This contour can be split into two contours defined by $\gamma_I^+ = \{\lambda \in \gamma_I \,|\, \Im(\lambda) \geq 0\}$ and $\gamma_I^- = \{\lambda \in \gamma_I \,|\, \Im(\lambda) < 0\}$ ($\Im$ denotes the imaginary part) as seen in Fig. 1. As γ_I^+ and γ_I^- are followed in opposite directions and as they are complex conjugates, we obtain:

$$P_I = \frac{1}{2\,i\,\pi} \int_{\gamma_I^+} [(L + \lambda)^{-1} - (L + \overline{\lambda})^{-1}]\, d\lambda = \frac{1}{\pi} \int_{\gamma_I^+} \Im(L + \lambda)^{-1}\, d\lambda$$

and then, taking the integral kernel of this expression,

$$[\![P_I]\!] = \frac{1}{\pi}\int_{\gamma_\varepsilon^+} \Im[\![(L+\lambda)^{-1}]\!]\, d\lambda$$
$$= -\frac{1}{\pi}\int_{\omega_-}^{\omega_+} \Im[\![(L+(\omega+i0)^2)^{-1}]\!]\, 2\,\omega\, d\omega$$

which leads to the Stone formula, using the definition of $\hat{G}$

$$[\![P_I]\!](\vec{r}_1,\vec{r}_2) = -\frac{2}{\pi}\int_{\omega_-}^{\omega_+} \omega\, \Im\hat{G}(\omega,\vec{r}_1,\vec{r}_2)\, d\omega$$

This formula gives, by taking the derivative with respect to ω_+,

$$\frac{d}{d\omega_+}[\![P_I]\!](\vec{r}_1,\vec{r}_2) = -\frac{2\,\omega}{\pi}\,\Im\hat{G}(\omega,\vec{r}_1,\vec{r}_2) \tag{8}$$

The combination of equation 7 and equation 8 finally gives:

$$\hat{C}(\omega,\vec{r}_1,\vec{r}_2) = -\frac{2^{d+1}\,\pi^{d-1}}{\sigma_{d-1}}\,\frac{c^d}{\omega^{d-2}}\,\Im\hat{G}(\omega,\vec{r}_1,\vec{r}_2) \tag{9}$$

This gives a generalization of equation 5 in the case of observation in a region without local sources, and requires no hypothesis about attenuation. It shows that the equipartition at boundaries of the region of interest is sufficient to obtain the Green's function from cross-correlation, whateveris the wavefield inside the medium is. This equation, established in the scalar case, can be extended to the elastic case using the same calculation. The cross-correlation function becomes a tensor, as well as the Green's function. Particular attention needs to be paid to velocities and dispersion relations as they depend on the type of waves.

The rate of convergence towards the Green's function

The question arises as to how much averaging is in principle necessary after which the Green's function is retrieved, and before which the cross-correlation remains dominated by noise. In the case that the field is due to uniformly distributed random sources, or in the case that the field is due to equipartitioned incident waves, it is possible to make theoretical estimates (Larose *et al.* 2004; Snieder 2004; Sabra *et al.* 2005c; Weaver and Lobkis 2005a). All these authors have concluded, not surprisingly, that the convergence proceeds like the square root of the amount of data used in the cross-correlation. signal-to-noise ratio, i.e. Green's function amplitude over residual fluctuations, is proportional to this square root. Quantitative estimates of the quality of the convergence are more challenging. Weaver and Lobkis (2005a) calculated the residual error in a scalar wave cross-correlation, and found it to be proportional to the energy in the diffuse field times the bandwidth times the fourth power of central frequency. A similar calculation for closed systems was confirmed in laboratory measurements (Weaver and Lobkis 2005b). The residual error was compared to the amplitude of a ray arrival expected in the converged cross-correlation. Each ray arrival amplitude A depends on 1) the geometrical spreading of the Green's function, and 2) the spatial extension of the noise sources that coherently contribute to the Green's function reconstruction. This zone is characterized by a directivity angle $\delta\theta = \sqrt{\frac{c}{r\,\omega}}$, where r is the source-receiver distance. The ray arrival was shown to be apparent in the cross-correlation if $\delta t\,\delta\omega \gg A^{d-1}$, where δt is the amount of data record employed (this is often months in seismic applications), $\delta\omega$ is the bandwidth of interest (often around 1 Hz or less in seismic applications), and $A = r\omega\,/\,c$, (the source-receiver distance r times the wavenumber $k = 2\pi\,/\,\lambda$). The power is equal to one less than the dimension d of the propagation; thus $d-1=1$ for Rayleigh waves. Propagation between distant source-receiver pairs, and propagation in three dimensions, are especially challenging to resolve, largely due to the weakness of such ray arrivals.

SURFACE WAVE TOMOGRAPHY OF EUROPE

Practically, cross-correlation can be used at different scales to image structures from noise. Here, we present an example of seismic noise processing to produce high-resolution Rayleigh and Love waves group velocity maps for a region surrounding the European Alps. We focused on the [5–50 s] period band, where surface waves are mostly sensitive to the crust.

Stehly *et al.* (2006) have shown that the seismic noise sources in the [5–20 s] period band cover a large surface when integrated over a long time. This allows us to retrieve the Green's function between two stations by correlating background seismic noise records. The emerging signal of the noise correlation function is dominated by surface waves, since the background seismic noise mainly consists of surface waves. The reconstructed Green's functions are stable over time and robust enough to measure surface wave propagation times with a precision of a few tenths of a second, independently of the azimuth of the considered station pair path (Stehly *et al.* 2007).

Passive imaging from seismic noise and Rayleigh wave group velocities was first used by Shapiro *et al.* (2005) and Sabra *et al.* (2005a) who provided images of the Californian crust. More recently, noise based surface-wave tomography has been applied in Tibet (Yao *et al.* 2006), New Zealand (Lin *et al.* 2007) and Korea (Kang and Shin 2006) and to produce large-scale Rayleigh wave group velocity maps across Europe (Yang *et al.* 2007).

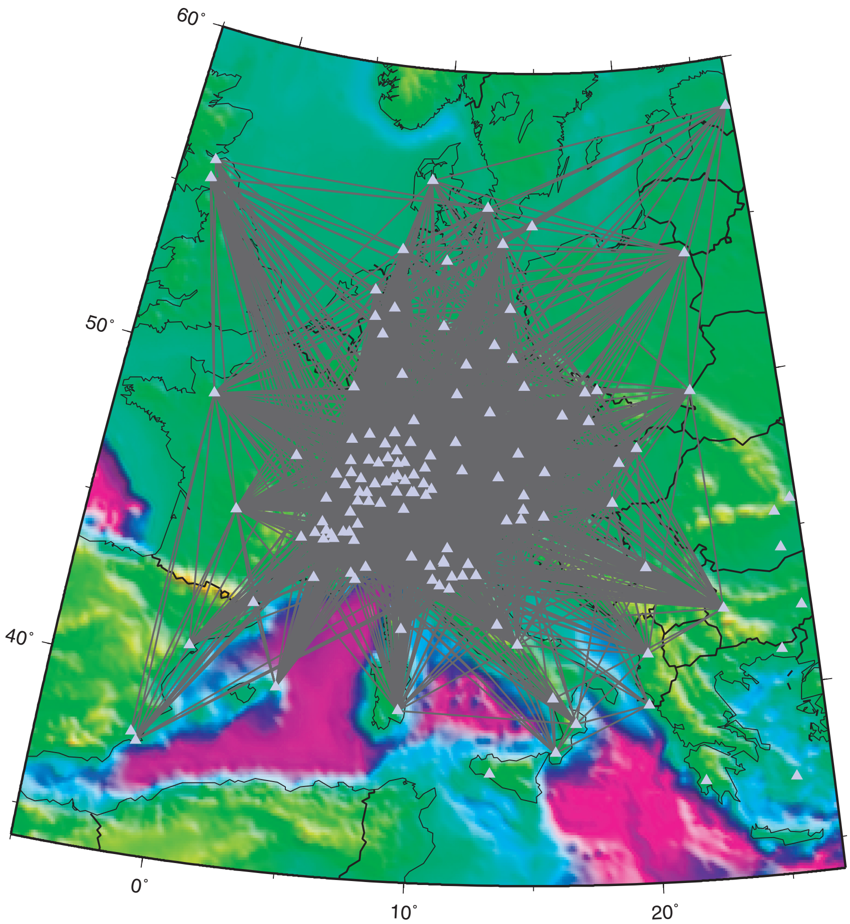

Figure 2 The 3000 selected paths where 16 s Rayleigh wave group velocity measurements were obtained from cross-correlations of ambient seismic noise. White triangles show stations used for this study.

We used one year of continuous records from October 2004 to October 2005 from 150 3-components broadband European stations. Our aim is to focus on the Alps, where we have a particularly high density of stations (Fig. 2). All the records are processed day per day. First the data are decimated to 1 Hz and corrected for the instrumental response. North and east horizontal components are rotated to obtain radial and transverse components with respect to the inter-station azimuth. The records are then band-pass filtered and their spectrum whitened between 5 and 150 s. We correlated signals recorded on the components that correspond to the non-zero terms of the theoretical elastic Green's tensor (ZZ, ZR, RZ, RR, and TT, due to symmetry considerations). Subsequently, correlations of one-day records are stacked. This is approximately equivalent to cross-correlating directly the whole year of records.

Rayleigh and Love waves dispersion curves are evaluated from the emerging Green's function using frequency-time analysis (Levshin *et al.* 1989; Ritzwoller and Levshin 1998) for the 17,000 inter-station paths. For each path we obtain eight evaluations of the Rayleigh-wave dispersion curves by considering four components of the correlation tensor (ZZ, RR, RZ and ZR) and both the positive and the negative part of the noise correlation function. Similarly, we obtain two estimates of the Love-wave dispersion curves from positive and negative parts of TT correlations.

We reject waveforms 1) with signal-to-noise ratio (ratio between Rayleigh wave's amplitude and noise variance after it) lower than seven; 2) with group velocities measured on the positive and negative correlation time differing by more than 5 percent; and 3) with paths shorter than two wavelengths at the selected period for the group velocity map. This results in about 3,500 paths over the initial 11,000 inter-stations paths at 16 s (Fig. 2). We then apply a tomographic inversion following Barmin *et al.* (2001) to this data set to obtain group velocity maps on $100 \times 100 = 10{,}000$ cells of 25×25 km

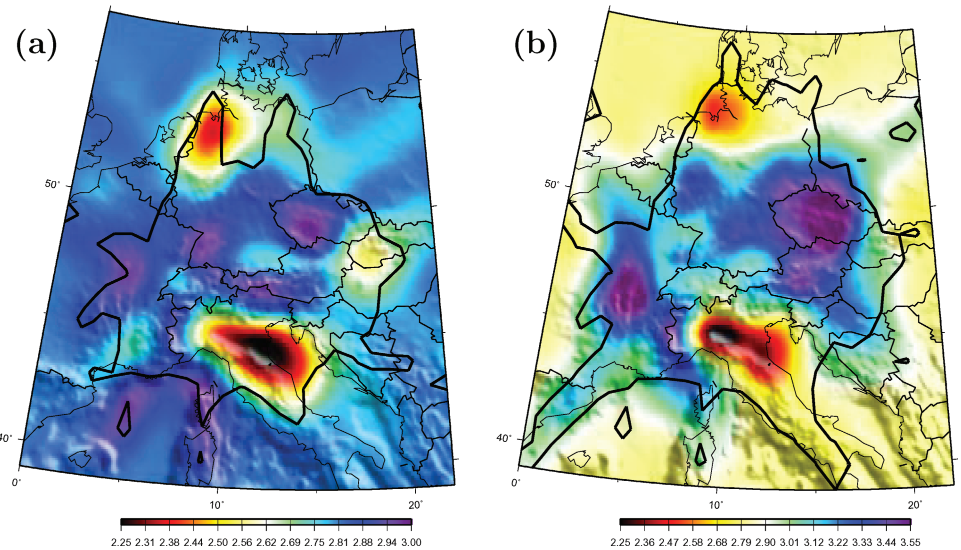

Figure 3 Rayleigh (a) and Love (b) wave group velocity maps at 16 s period constructed from 3,500 and 4,400 inter-station cross-correlations, respectively. Black thick line delimits the area where there are more than 10 paths per 25 × 25 km cell.

across Europe (Fig. 3). Several geological features can be seen on those maps. Low velocity anomalies are associated with sedimentary basins, such as the Po basin (Northern Italy), the North Sea basin and the Pannonian basin (Slovakia and Hungary). Both Rayleigh and Love waves exhibit smaller values below the molassic sediments (Southern Germany and Austria) than in the surrounding area. Close to the French-Italian border, one can notice a high-velocity anomaly corresponding to the Ivrea body, an intracrustal high- velocity and high-density zone within the Adriatic plate. The final resolution is good enough to see the contrast in Rayleigh wave velocity between the sedimentary (north-west) and the mountainous (south) part of Switzerland.

It is not possible to compare directly these group-velocity maps with maps obtained by active methods: practically, below 20 s of period, attenuation as well as scattering in the medium are too strong, preventing accurate measurement of surface-wave velocity from earthquakes or any active source. At these periods, the number of usable paths is thus too low to build any group-velocity map.

It is however possible to compare dispersion curves measured from passive and active methods in some other cases. Shapiro and Campillo (2004) measured dispersion curves using noise cross-correlation computed between pairs of stations separated by distances ranging from one hundreds to two thousand kilometres. At periods below 60 s, the resulting dispersion curves are in good agreement with those predicted by global group-velocity maps from Ritzwoller *et al.* (2002). In Southern California, Shapiro *et al.* (2005) compared records of an earthquakes which occurred close to a station and recorded at two other stations, with noise cross-correlation signal computed on the same path. The measured arrival time was identical at the period ranging from 5 to 20 s. These results shows the robustness of measurements performed using noise cross-correlations.

The Alpine region has intensively been studied using controlled source and earthquake tomography. These studies gave precise insight about the crustal and upper mantle structure (Marchant and Stampfli 1996; Waldhauser *et al.* 1998, 2002; Bleibinhaus and Gebrande 2005 and references therein). However, using seismic noise instead has several advantages. The final resolution depends mostly on the density of stations and is not limited by the available sources. This makes it possible to obtain high-resolution group velocity maps that cover large regions, whereas controlled sources can only be used for small areas. Surface wave tomography using earthquakes records only provides group velocity maps at periods above 20 s, since all the high- frequency information is lost due to attenuation in the medium.

3D S-WAVE TOMOGRAPHY OF THE PITON DE LA FOURNAISE VOLCANO

The same seismic noise cross-correlation technique can be applied to study more complex structures. In this section we present the 3D velocity model of a volcano obtained using only noise records.

Eighteen months (July 1999 to December 2000) of continuous seismic noise recorded at 21 vertical short period stations were collected by the Observatoire Volcanologique du Piton de la Fournaise (Fig. 4a). An example of a noise record at one of the stations (ANR) is shown in Fig. 4b. All noise records are first band passed between 1 to 5 s and their spectral amplitudes whitened in order to avoid strong dominant spectral peaks in the background noise.

For each available station pair, the one-bit noise correlation function is computed day per day. Some of the noise correlation functions are rejected upon a signal-to-noise ratio criterion (i.e. if the energy of the Rayleigh arrival is lower than 1.5 times the energy of the noise). The remaining traces are stacked over 18 months. For each path, group velocity dispersion curves are estimated using a frequency-time analysis (Levshin *et al.* 1989; Ritzwoller and Levshin 1998). We manually select dispersion curves according to group velocity limits and for station-to-station distances longer than one wavelength. We finally obtain 75 reliable dispersion curves from which group velocities are extracted for periods equal to 2, 2.5, 3, 3.5, 4 and 4.5 s.

The 2D Rayleigh wave group velocity maps are obtained from tomographic inversion of the arrival-time measurements at each period using the algorithm described by Barmin *et al.* (2001). Our 2D models involve $22 \times 28 = 616$ 1×1 km cells. Because of the sparse ray coverage and the low resolution of the data set, we choose to apply a strong smoothing to the tomographic inversion which results in a ~4-km spatial resolution. The inversion results are thus robust and show a moderate variance reduction varying from 38 to 18% with increasing periods (from 2 to 4.5 s).

Dispersion curves are then extracted from the Rayleigh-wave group-velocity maps for every model cell. We fit these curves by polynomial functions in a least-squares sense and invert them using a Monte-Carlo algorithm (Shapiro *et al.* 1997), the synthetic dispersion curve being calculated using a method due to Herrmann (1987). We thus obtain a S-wave velocity-versus-depth profile for each cell. We present six horizontal slices as well as a 3D view of the 3D smoothed model in Figure 5. The results clearly show the presence of a high-velocity anomaly which moves westward with depth (+1.3 to −1.1 km above sea level). This structure is surrounded by a low-velocity ring interpreted as effusive products associated with the construction of the Piton de la Fournaise volcano on the flank of the older Piton des Neiges volcano. This high-velocity anomaly has also been detected by a previous earthquake and active P-wave tomography on the Piton de la Fournaise volcano (Lankar 1997). Recent works also imaged

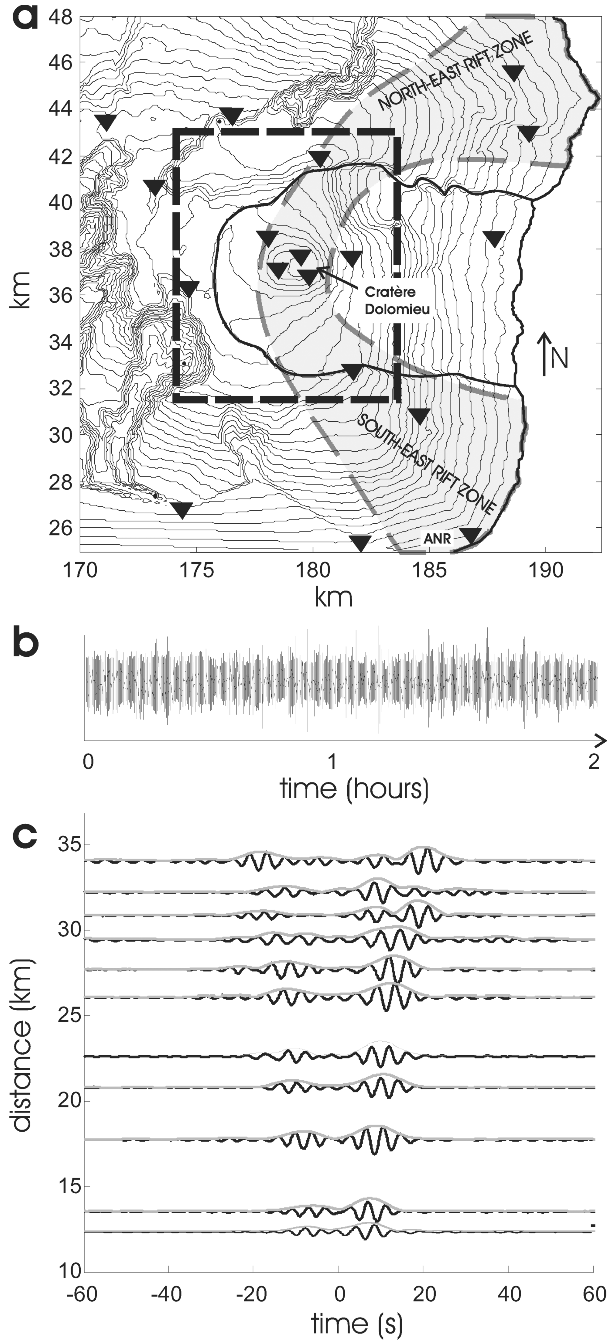

Figure 4 **a**. Map of the Piton de la Fournaise volcano. Seismic stations are represented as inverted triangles. The gray zone indicates the limits of the rift zone. The thin dashed rectangle corresponds to the limits of the presented tomographic images. Geographic coordinates are Gauss-Laborde kilometric coordinates (Transverse Mercator). Contour lines are spaced every 100 m. **b**. Two hours of ambient seismic noise at station ANR. **c**. Causal and acausal reconstructed Rayleigh waves (positive and negative times, dominant period 4 s) between station RMR (not shown on the map) and the rest of the network. The trace envelopes are represented as thin gray curves.

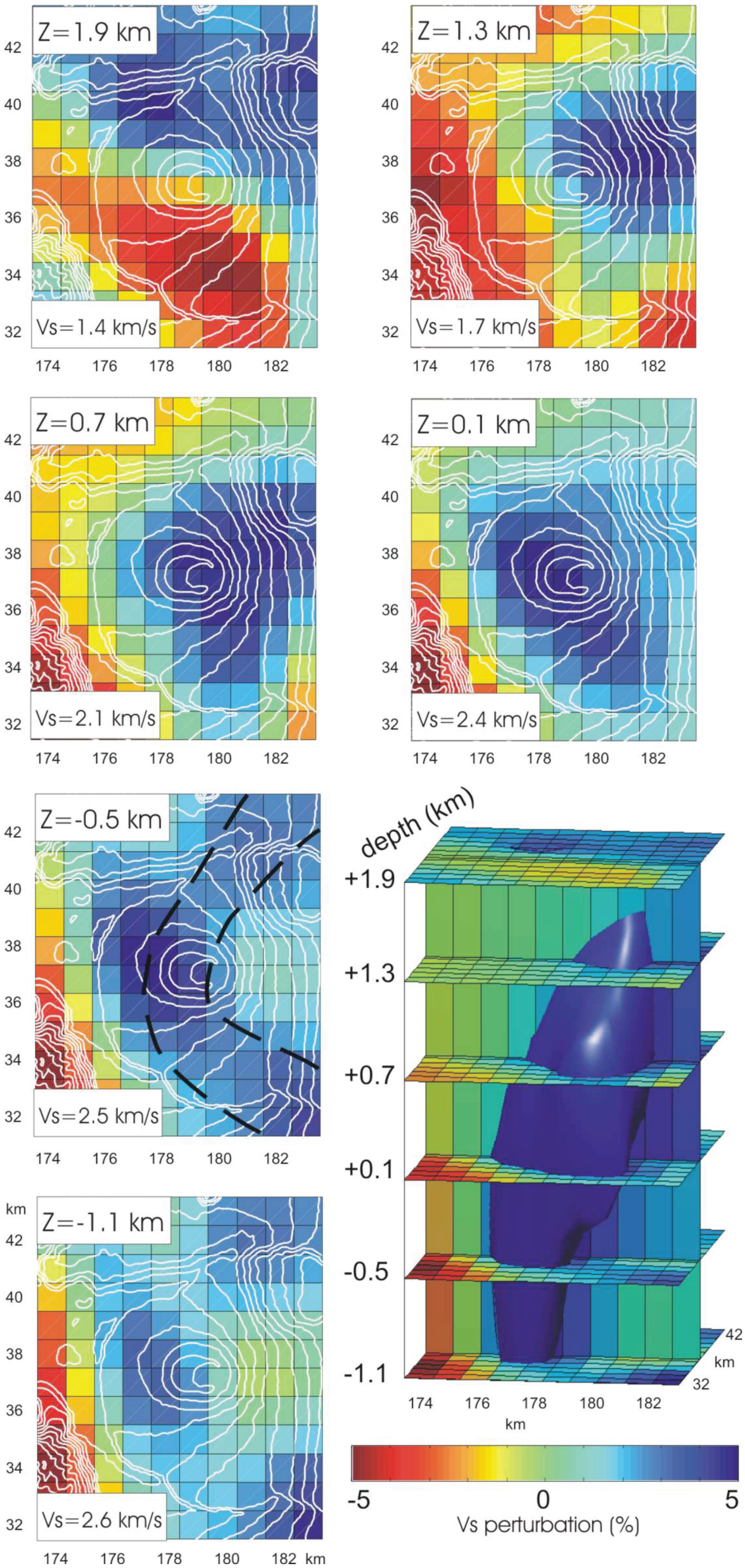

Figure 5 3D S-wave velocity model. We show 6 horizontal slices extracted from the 3D model at different depths. Average S-wave velocity is shown in white boxes on the bottom of corresponding slices. Black dashed line at depth −0.5 km shows the limits of the rift zone. We also plot a 3D view of the model. The 3D blue patch delimits the iso-velocity perturbation surface corresponding to a 2.5% velocity perturbation.

the presence of a high-velocity chimney on different volcanoes (Laigle *et al.* 2000; Tanaka *et al.* 2002; Zollo *et al.* 2002; Sherburn *et al.* 2006; Patan *et al.* 2006). We interpret this anomaly as solidified intrusive magma bodies. The high-velocity anomaly is also well correlated with the rift zone at sea level ($z = -0.5$ km). Imaging these intrusive bodies is of particular interest because the magma paths are usually believed to follow their geometry (Laigle *et al.* 2000; Battaglia *et al.* 2005). Furthermore, other studies showed that a few months of seismic noise data will yield similar three-dimensional results to that obtained from 18 months' data (Brenguier *et al.* 2008). We also achieved a preliminary study on the temporal variations of the reconstructed Green's functions showing that we could detect relative velocity variations of less than 0.1% with a temporal resolution of one day.

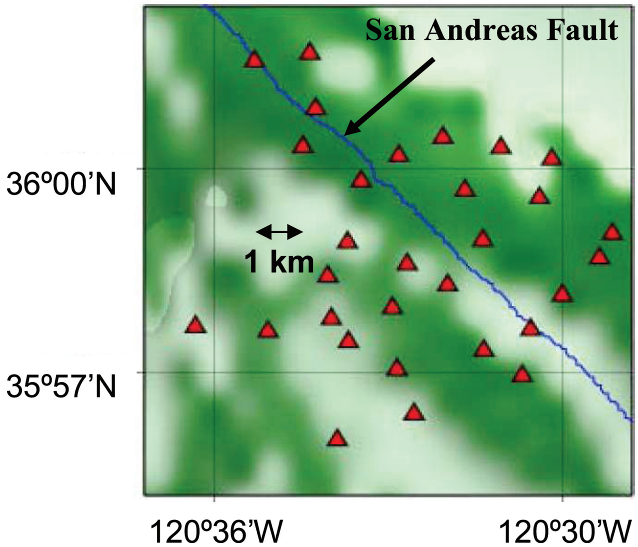

Figure 6 Topographic map of the Parkfield area (an 11-km large square) showing stations (triangles) and SAF (blue).

P-WAVES EXTRACTION FROM SEISMIC NOISE CROSS-CORRELATION

A main issue in the convergence of the correlation process to the transfer function is the influence of variations in the temporal and spatial distribution of the noise sources. From the temporal point of view, the noise spectrum defines the frequency bandwidth over which the impulse response can be retrieved. When receivers are widely separated, the coherent propagating noise must have sufficient amplitude to be recorded on both receivers despite geometrical spreading and attenuation. This explains why the slowly-attenuated Rayleigh waves have dominated the impulse response obtained so far from correlations of seismic noise.

In this section, we present results from the correlation function of seismic noise recordings among pairs of stations in the dense Parkfield network, California. When performed on many station pairs at short ranges, the noise correlation function demonstrates the presence of both a P-wave and a Rayleigh wave in the noise correlation function.

We processed data recorded on the dense temporary seismic network installed in the Parkfield area between July 2001 and October 2002. One month of seismic noise recordings were cross-correlated between each pair of 30 broadband 3-component seismic stations located in an 11-km square (Fig. 6, Thurber *et al.* 2004). We used only the vertical component. This network has extensively been used to monitor and image the San Andreas Fault using both man-made explosions and earthquakes as part of the San Andreas Fault Observatory at Depth (SAFOD) project. Inversion results have confirmed the spatial heterogeneity of P-wave velocity across the Fault up to 6 km in depth (Ben-Zion and Malin 1991; Catchings *et al.* 2002; Hole *et al.* 2006).

At first, frequency-incoherent beamforming is performed using the N = 30 stations of the network to determine the average velocity c and direction θ of the seismic noise (Fig. 7). Beamforming is performed in two frequency bands of interest [0.2–0.5 Hz] and [0.6–1.3 Hz], on data segments of one day of seismic noise,which were recorded in February 2002, as:

$$B(\theta, c) = \frac{1}{\delta\omega} \int_{\omega_c-\delta\omega/2}^{\omega_c+\delta\omega/2} \sum_{i=1}^{N} \hat{S}_i(\omega) \exp\left(i\frac{\omega}{c}(x_i \sin\theta + y_i \cos\theta)\right) d\omega$$

where ω_c is the central noise frequency and $\delta\omega$ the frequency bandwidth, $\hat{S}_i(\omega)$ is the complex Fourier component at frequency ω of the noise signal $S_i(t)$ recorded on the ith seismic station ($i \in [1, N]$), and (x_i, y_i) are the longitude/latitude coordinates of station i. Working with a dense seismic network having a small coverage area allows determination of an average apparent incoming velocity for this zone using plane wave beamforming. In both of the frequency bands, the noise field clearly originates from the Pacific Ocean with an incident direction $\theta_0 = 55°$ on the Parkfield network. On the other hand, the beamformer in the [0.2–0.5 Hz] band exhibits an apparent velocity of 2.8 km/s compatible with a Rayleigh wave (Fig. 7a), while the beamformer in the [0.6–1.3 Hz] band shows an apparent velocity of 5 km/s (Fig. 7b).

Since Fig. 7 reveals a strong directivity in the seismic noise, only station pairs aligned with the noise main direction θ_0 are

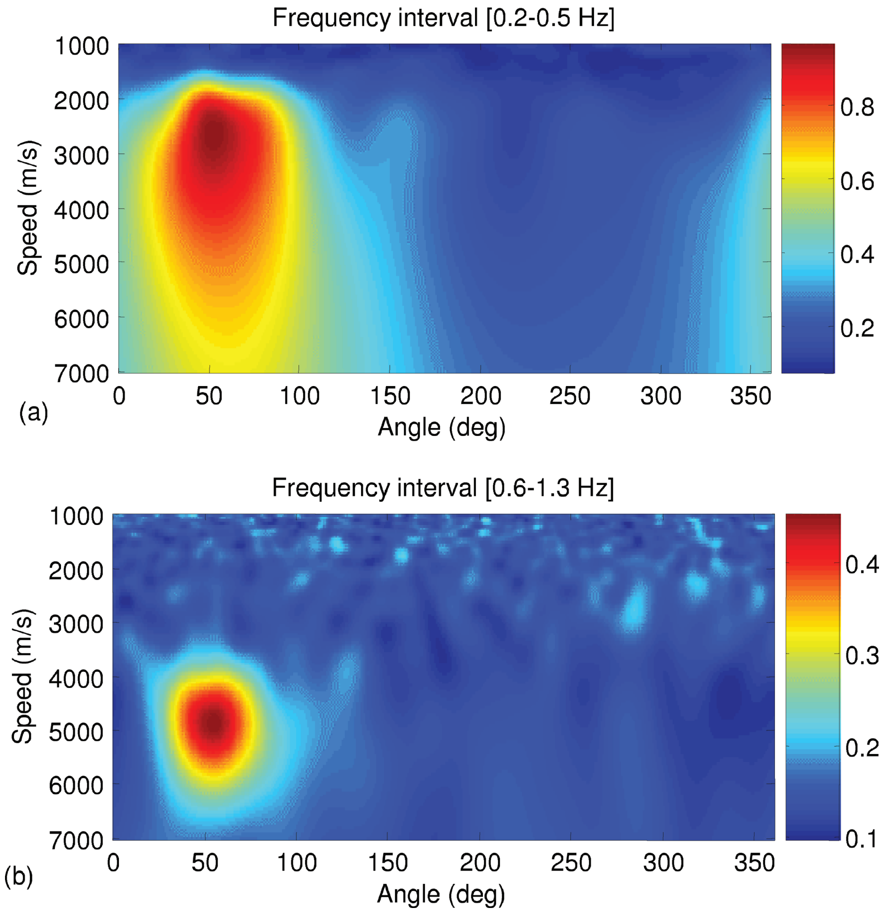

Figure 7 Angular-speed distribution of pre-processed incoming noise on the Parkfield network averaged over one month. Plane wave beamforming is summed incoherently over 100 frequencies from (a) 0.2 to 0.5 Hz and (b) 0.6 to 1.3 Hz. The x-axis corresponds to noise directivity θ, north is 0°.

chosen to compute the point-to-point noise correlation function. Restricting the cross-correlations to these pairs ensures that 1) the travel time of the main peak of the noise correlation function is not biased and corresponds to the actual travel time of the Green's function between the stations (Snieder 2004; Roux *et al.* 2005b) and 2) the signal-to-noise ratio of the noise correlation function is maximized. Practically speaking, 145 station pairs are selected in the Parkfield network whose angles θ_{ij} are included in a directivity angle $\delta\theta = |\theta_{ij} - \theta_0| \le \sqrt{\frac{c}{R_{ij}\,\omega_c}}$ dependent on the distance R_{ij} between stations and the frequencies characteristics of the seismic noise field (Roux and Kuperman 2004).

The noise correlation function is computed for each selected station pair as in equation 3 of Section 2, and averaged over 30 days to further increase the signal-to-noise ratio. Figure 8a is a display of the noise correlation functions obtained for the 145 selected pairs sorted by ascending offset R_{ij}. A propagating wavefront clearly appears at high frequency (Fig. 8b) which corresponds to a ~5 km/s velocity wave. A polarization study between the Z-R and Z-Z components of the correlation tensor confirmed the P-wave nature of this wavefront (Roux *et al.* 2005a).

Going back to Fig. 7(b), we note that the apparent velocity of the P-wave corresponds to the P-velocity at the turning point. Recent inversions of the P-wave velocity profile reveal a strong velocity gradient at the surface, the 5 km/s speed being reached at no more than 1.5 km in depth on the west side of the San Andreas fault. This confirms that the noise sources that excite P-waves are local and cannot be confused with deep incident waves that would hit the seismic array with a much higher apparent velocity. One hypothesis is that P-waves are locally generated by conversion of incident Rayleigh waves coming from the Pacific by local heterogeneities at the Earth's surface or subsurface.

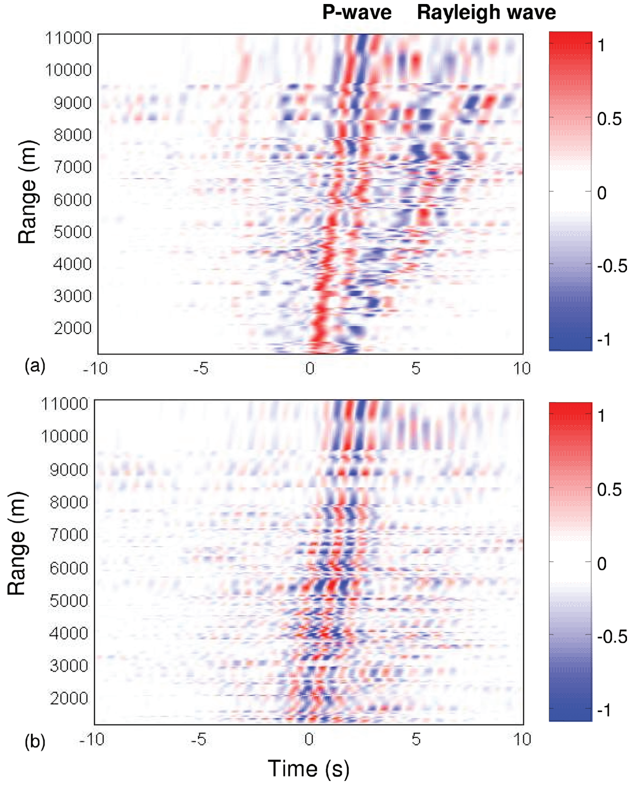

Figure 8 Range-time representation of the Z-Z component of the noise correlation tensor averaged over one month in two frequency bands (a) [0.1–1.3 Hz], and (b) [0.6–1.3 Hz]. Each plot has been normalized by its own maximum.

SMALL SCALE GEOPHYSICS USING SURFACE WAVES EXTRACTED FROM NOISE CROSS-CORRELATION

In this section, we achieve an experimental demonstration of the correlation process of controlled noise sources at the metre scale using a linear array of accelerometers. It is known that the cross-correlation of seismic noise between two receivers converges towards the Green's function when noise is equidistributed in azimuth. The same result can be obtained with directional noise if noise sources are located in the end-fire lobes centered along the array line direction (Roux and Kuperman 2004). When noise is not isotropic and noise sources are not adequately located with respect to the receivers array, 'controlled' noise sources can be used to produce appropriate wavefield satisfying the end-fire lobe criterion. This is particularly useful at small scales and high frequencies where local sources strongly contribute to the noise wavefield.

A 14-metre long line of 8 evenly-spaced vertical accelerometers has been used to record human steps. We walked in the alignment of the accelerometers line, 5 times one minutes on each side, from 0 to about 30 metres away from the accelerometer array. The experimental setup was designed to be versatile: 1) the array configuration may include up to 16 one-component seismic stations; 2) these seismic sensors could be accelerometers or geophones depending on the expected frequency bandwidth; 3) the array length is adjustable to the surface wave wavelength.

The main advantage of this system is to be easy and fast to setup. Our ambition was to achieve a complete deployment, acquisition and processing in approximately 30 minutes. The system design makes it very convenient for local and near surface measurements.

The energy spectrum of the recorded steps spreads up to 150 Hz. Given the frequency response of the accelerometers and the spatial extension of the array, a frequency interval ranging from 10 to 100 Hz was selected for the analysis. Since the frequency spectrum of the steps is not flat in this frequency interval, and as correlating is mathematically equivalent to a spectrum product, only the most energizing frequencies will emerge in the correlation signal. To enlarge the effective frequency bandwidth, the spectrum of the records is equalized in the selected frequency interval [10–100 Hz] before the correlation process.

To check the robustness of the correlation process, five one-minute long records were separately correlated for each accelerometer pair. The five time-domain correlations superimpose in phase, leading to the conclusion that correlation is robust and does not depend on the way we walked. As these correlation signals superimpose, they are stacked to increase the signal-to-noise ratio. The advantage of the correlation process is then to perform an ensemble average over the 'controlled' noise sources without the need of synchronization. The superposition of the correlations of one minute long signals is thus just a verification of the repeatability of the steps. Stacking five correlations of one minute long records is equivalent to correlating directly a 5-minute long signal.

To obtain a seismic section from the correlation process, signals are cross-correlated by the accelerometers located at the extremity of the line array. Taking one or the other of the accelerometers as the reference signal does not modify the seismic section. This shows that seismic propagation from left to right is identical to propagation from right to left on the 14-m long seismic array. The medium can then be assumed 1D in the frequency bandwidth of the recordings. The 1D argument can be pushed even further. Two receiver pairs separated by the same range are stacked since propagation does not depend on the pair location but only on the offset between receivers.

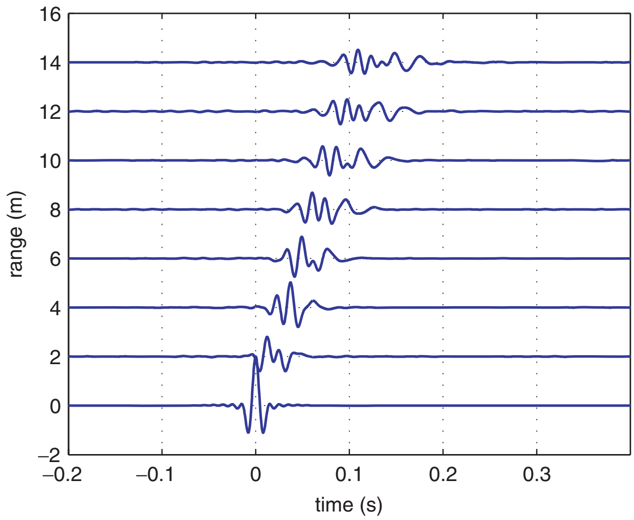

Figure 9 Seismic section obtained from the correlation process after all averaging operations. The signal-to-noise ratio is above 30 dB for each trace. Both phase dispersion and attenuation are observed. The seismic propagation reveals the presence of two surface waves with group velocity of about 90 and 120 m/s.

Figure 9 shows the seismic section obtained after the complete spatial and temporal stacking. After a 10-minutes total recording, signal-to-noise ratio is above 30 dB. Both phase dispersion and attenuation during propagation is retrieved. The final seismic section clearly reveals the presence of two surface waves, with mean group velocities of about 90 and 120 m/s. Those low group velocities are good indications of two Rayleigh modes.

We wish to insist on the fact that this section was obtained from 10 minutes of unsynchronized human steps only, which makes it almost a passive method. To obtain the same result with usual active seismic techniques, much more time would have been needed to synchronize numerous sledgehammer blows. The 'passive' method presented here is thus 1) easy to implement, as there is a large flexibility in the array configuration, 2) fast, as it takes only about 30 minutes to complete the array deployment and the recording, and 3) simple, as there is no synchronization task and processing is performed in real time.

A frequency-wavenumber (F-K) transform was applied to the seismic section in Fig. 9 to identify each of the surface waves (Fig. 10). As the accelerometers are evenly spaced by a distance $d = 2$ m, the largest wavenumber before aliasing is $2\pi/d = \pi$. In Fig. 10, this value of k corresponds to the green line. Higher k's are wrapped, and appear as low wavenumbers. In this simple case, the wavenumber spectrum can be extended by unwrapping the k axis.

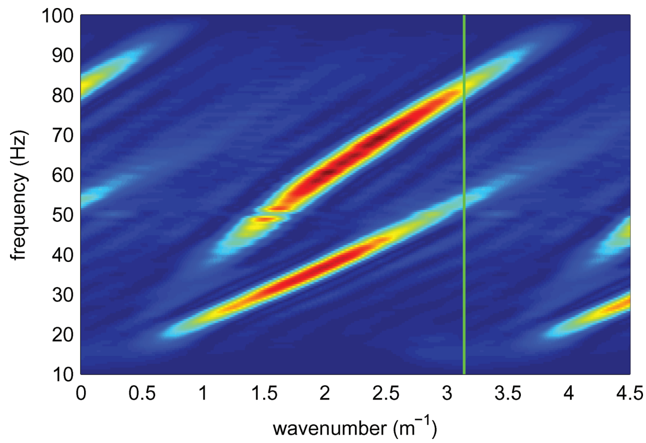

Figure 10 Frequency wavenumber (F-K) transform of the seismic section obtained in Fig. 9. The largest measurable wavenumber according to the Shannon criterion is $2\pi/d$ with $d = 2$ m (green line). The aliasing in the F-K diagram is resolved by unwrapping the k axis. The shape of the two modes on the F-K diagram reveals dispersive modes.

From the F-K diagram in Fig. 10, modes are separated and their phase velocity dispersion curves are extracted. Those surface-wave dispersion curves are the starting point for a surface wave inversion to retrieve the local velocity versus depth profile of the medium.

PASSIVE CORRELATION IMAGING OF A BURIED SCATTERER

Up till now, most of geophysical applications of passive imaging with ambient-noise cross-correlation have been used to reconstruct direct arrivals of Rayleigh or P-waves. Reconstructing other features of the Green's function, like the reflections following direct waves, is harder: the reflections are weaker and the propagation is fully 3D. Nevertheless, passively imaging a scatterer would form a major application to prospecting and certainly deserves attention. In order to test the feasibility of passively imaging a buried scatterer, we set a controlled ultrasonic experiment in the laboratory. We believe the principles presented here also apply to ambient seismic noise.

To mimic micro-seismic vibrations, we use a highly reverberant body excited by a series of sources (see Fig. 11). A 12 mm diameter cylindrical hole was drilled through an aluminium block of dimensions 125 mm × 125 mm × 90 mm. The hole is 25 mm beneath the surface. To excite elastic waves, we employ a laser mounted on a step motor. For a complete description of the experimental set-up, please refer to Larose *et al.* (2006b). The laser emits mainly shear waves (Mason and Thurston 1988) (see directivity in Fig. 11). The resulting

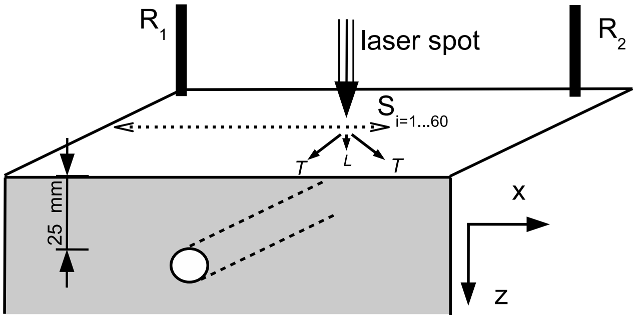

Figure 11 Set-up of the ultrasonic experiment. The source scans the surface with 1 mm steps along a line of 60 mm. The directivity (Mason and Thurston 1988) of one laser shot is shown for shear (transverse *T*) waves, and weaker compressional (longitudinal *L*) waves.

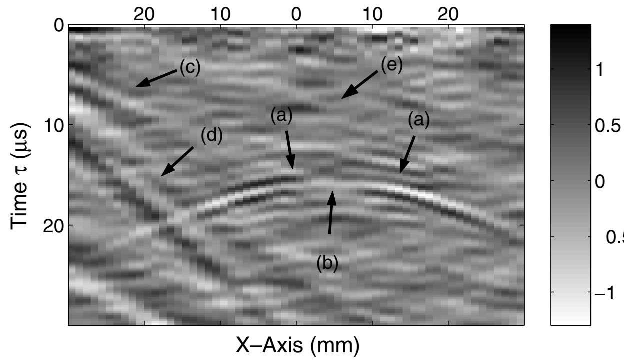

Figure 12 Time-distance wavefield (linear scale, arbitrary unit). Each autocorrelation $C_{ii}(\tau)$ is plotted for different position i along the X-axis, and time τ. Position 0 marks the center of the array; (a-e) are different reflections (see the text).

wave field is recorded by two pin transducers located at $\vec{r}_1$ and $\vec{r}_2$. The laser triggers the waveform acquisition. For each position of the source $\vec{r}_s^{\,i}$ and receiver k, the record is noted $S_{ik}(t) = G(t, \vec{r}_k, \vec{r}_s^{\,i}) \otimes R_k(t)$ where G is the elastic Green's function, $\otimes$ is convolution and $R_k(t)$ is the transfer function of the receiver k. Each record is filtered in the [0.05–0.9 MHz] frequency band, where the absorption time of the block is about 30 ms. Diffuse field decay is therefore slow enough to permit record lengths greater than 100 ms, which represents thousands of reverberations within the cavity. After each acquisition, the laser is moved to another position. 1 mm steps are used to mimic a linear array of 60 points. By reciprocity, the sources and receivers can be interchanged. Our experimental set-up is therefore analogous to a conventional seismic experiment where a linear array of 60 geophones would sense the seismic diffuse wavefield generated by two distant sources. The Green's function between any couple of points $(\vec{r}_s^{\,i}, \vec{r}_s^{\,j})$ of the array is recovered by processing the following time-correlation:

$$C_{ij}^k(\tau) = \int S_{ik}(t)\, S_{jk}(t+\tau)\, dt$$
$$= G(t, \vec{r}_k, \vec{r}_s^{\,i}) \times G\left(t, \vec{r}_k, \vec{r}_s^{\,j}\right) \otimes R_k(t) \otimes R_k(-t)$$

To remove the receiver functions R_k, we deconvolve the cross-correlations by the averaged auto-correlations $\langle C_{ii}^k(\tau)\rangle_i \approx R_k(t) \otimes R_k(-\,t)$. This procedure has the additional virtue of removing contaminations $G(t, \vec{r}_k, \vec{r}_k)$ or *ghosts*, which Derode *et al.* (2003b), Weaver and Lobkis (2006) related to the environment of the receivers R. Then these correlations are averaged over the available distant sources $\vec{r}_{k=1,2}$ to obtain $C_{ij}(\tau)$. As noted by several authors this correlation is essentially the Green's function $G(\tau, \vec{r}_s^{\,i}, \vec{r}_s^{\,j})$ and therefore should contain the deterministic signature of the isolated scatterer.

In Fig. 12 we display the time-distance wavefield obtained for all the available autocorrelations $C_{ii}(\tau)$. This autocorrelation is the field sensed in i if i were both source and receiver. Position 0 marks the centre of the array. The hyperbolic feature is the signature of the buried scatterer: the wave labeled (a) is the wave reflected by the top of the cylindrical hole placed at $z = 25$ mm and $x = 4$ mm. The arrival times along the array correspond to a shear (transverse) wave ($v_T = 3.1\,\mathrm{mm}/\mu s$). (c) is a compressional-to-Rayleigh reflected by the lateral edge of the cavity, and (d) is a Rayleigh-to-Rayleigh reflected by the same edge. The shear wave directivity of the laser generation is clearly visible in the null at (b). Because longitudinal wave generation is much weaker than that of shear waves (Mason and Thurston 1988), its reflection (e) is hardly visible.

A noteworthy point is that the passive reconstruction of any $G(\tau, \vec{r}_s^{\,i}, \vec{r}_s^{\,i})$ remains imperfect. The averaging used to construct the correlation is finite, leaving visible fluctuations in Fig. 12. To improve the quality of this image, one could increase the record length, or employ additional receivers $\vec{r}_k$ (Weaver and Lobkis 2005b). Alternatively, we could perform beamforming in order to take advantage of all the $C_{i\neq j}$ cross-correlations. Beamforming is a standard procedure to obtain medical or seismic (migrated) image. The new point is that here the impulse responses $C_{i\neq j}$ are obtained *passively*.

The image we now process is a 2D image of the reflectivity of the medium. The first step is to apply beamforming to the forward propagation to focus the wave on any point (x, y) in the medium. This is achieved by summing the time-delayed impulse responses $C_{ij}(\tau)$. The same beamforming technique is then applied to the wave back-propagation (from the focal

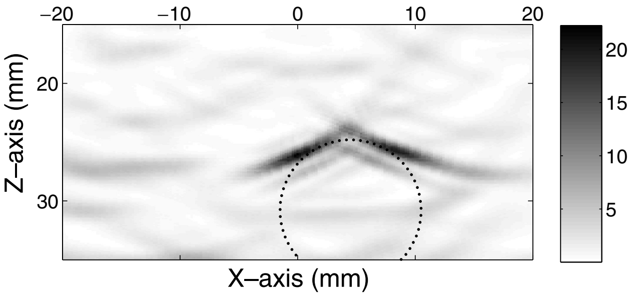

Figure 13 Reflectivity (linear scale, arbitrary unit) of the aluminium block as probed by bulk shear waves. The array of 60 laser sources is at $z = 0$. Black indicates a high reflectivity. The top of the hole is clearly visible. The actual position of the cylinder is displayed in the dotted line.

point to the receivers), the reflectivity ϕ of the medium is then:

$$\phi(x, y) = \left[\sum_{ij} C_{ij}(\tau_i + \tau_j) \right]^2$$

where $\tau_i = \frac{1}{v_T}\sqrt{(x - x_i)^2 + z^2}$ and v_T is the shear wave velocity. The 2D reflectivity map of the medium is displayed in Fig. 13. The top of the reflector is clearly visible. Because of the finite size of the linear array, the sides and bottom of the cylindrical hole cannot be imaged. The shear wave directivity of the laser spot induces a preferential reflection for oblique incidences; additionally, the images in Figs 12 and 13 show a null at apex. Speckle fluctuations are noticeable making these figures a little more noisy than the ones obtained with Rayleigh waves. This is expected since the field at the free surface is dominated by Rayleigh waves.

To conclude this part, we have shown here the feasibility of imaging small details of the medium (like a buried isolated scatterer) by means of the passive time-correlation technique. By reciprocity this experimental set-up is analogous to an array of seismic geophones sensing the diffuse wavefield originating from distant sources. We therefore believe this technique could be transposed and applied to geophysical prospecting, as well as to medical imaging. The use of fully developed diffuse field in a closed cavity is not a rigorous requirement for this imaging technique. It could in principle be replaced by any other diffuse field, like diffuse waves in an open medium, or ambient noise.

CONCLUSION

In this paper, we theoretically reviewed how and under which assumptions cross-correlation of noise recorded at two sensors yields the Green's function between them. This property is based on equipartition of the wavefield that can be provided either by an appropriate sources distribution or by wave scattering in the medium. Any diffuse field, like diffuse waves in an open medium, or ambient noise may be used to reconstruct the Green's function between two points.

We experimentally showed the feasibility of passive imaging using noise cross-correlation. This technique bypasses the usual shortcomings encountered in active imaging, especially concerning the requirements about sources (strength, location, occurrence, etc). Application to ambient seismic noise is particularly promising for improving images of the Earth as the number of usable ray paths for tomography is directly linked to the number of recording stations. In more complex structures like volcanoes, this technique was validated as the S-wave velocity model obtained presents the same anomalies as in active measurements. Nevertheless, in a context where standard active methods are hampered by irregular sources distribution, the possibility of using noise records is particularly interesting. These results demonstrate the possibility to achieve surface-wave tomography from noise cross-correlation. Results from the Parkfield area show that P-waves are present in the correlation on small-scale seismic networks, and could be used for body wave tomography.

At smaller scales, cross-correlation imaging techniques brings a new way to achieve seismic experiments that is faster and easier to implement than usual active methods. The recorded wavefield can be produced by active sources adequately located or using scattering to produce a diffuse wavefield. We showed that late arrivals, like reflections produced by buried objects, can be retrieved. This passive imaging of scatterers would be a major application of noise cross-correlation in geophysical prospecting. This technique is also promising for geophysical surveys, as seismic noise is a reproducible, stationary in time, natural source, that could also be used to give new insights into 4D seismic exploration.

REFERENCES

Aki K. 1957. Space and time spectra of stationary stochastic waves with special reference to microtremors. *Bulletin of the Earthquake Research Institute* **35**, 415–456.

Barmin M.P., Ritzwoller M.H. and Levshin A.L. 2001. A fast and reliable method for surface wave tomography. *Pure and Applied Geophysics* **158**, 1351–1375.

Battaglia J., Ferrazzini V., Staudacher T., Aki K. and Cheminée J.-L. 2005. Pre-eruptive migration of earthquakes at the Piton de la Fournaise volcano (Réunion Island). *Geophysical Journal International* **161**, 449–458.

Ben-Zion Y. and Malin P. 1991. San Andreas fault zone head waves near Parkfield, California. *Science* **251**, 1592–1594.

Bleibinhaus F. and Gebrande H. 2005. Crustal structure of the Eastern Alps along the TRANSALP profile from wide-angle seismic tomography. *Tectonophysics* **414**, 51–69.

Brenguier F., Shapiro N.M., Campillo M., Nercessian A. and Ferrazzini V. 2007. 3-D surface wave tomography of the Piton de la Fournaise volcano using seismic noise correlation. *Geophysical Research Letters* **34**, L02305.

Brenguier F., Shapiro N.M., Campillo M., Ferrazzini Z., Duputel Z., Coutant O. and Nercessian A. 2008. Toward forecasting volcanic eruptions using seismic noise. *Nature Geoscience*, in press.

Campillo M. 2006. Phase and correlation in 'random' seismic fields and the reconstruction of the Green function. *Pure and Applied Geophysics* **163**, 475–502.

Campillo M. and Paul A. 2003. Long-range correlations in the diffuse seismic coda. *Science* **299**, 547–549.

Catchings R.D., Rymer M.J., Goldman M.R., Hole J.A., Huggins R. and Lippus C. 2002. High-resolution seismic velocities and shallow structure of the San Andreas fault zone at Middle Mountain, Parkfield, California. *Bulletin of the Seismological Society of America* **92**, 2493–2503.

Claerbout J.F. 1968. Synthesis of a layered medium from its acoustics transmission response. *Geophysics* **33**, 264–269.

Colin de Verdière Y. 2006a. Mathematical models for passive imaging I: general background. URL http://fr.arxiv.org/abs/math-ph/0610043/.

Colin de Verdière Y. 2006b. Mathematical models for passive imaging II: effective hamiltonians associated to surface waves. URL http://fr.arxiv.org/abs/math-ph/0610044/.

Derode A., Larose E., Campillo M. and Fink M. 2003a. How to estimate the Green's function of a heterogeneous medium between two passive sensors? Application to acoustic waves. *Applied Physics Letters* **83**, 15, 3054–3056.

Derode A., Larose E., Tanter M., de Rosny J., Tourin A., Campillo M. and Fink M. 2003b. Recovering the Green's function from field-field correlations in an open scattering medium (L). *The Journal of the Acoustical Society of America* **113**, 2973–2976.

Duvall T.L., Jefferies S.M., Harvey J.W. and Pomerantz M.A. 1993. Time distance helioseismology. *Nature* **362**, 430–432.

Gilles P.M., Duvall T.L., Scherrer P.H. and Bogart R.S. 1997. A subsurface flow of material from the Sun equator's to its poles. *Nature* **390**, 52–54.

Godin O.A. 2007. Emergence of the acoustic Green's function from thermal noise. *The Journal of the Acoustical Society of America* **121**, EL96–EL102.

Gouédard P., Roux P. and Campillo M. 30 August - 01 September 2006. Small scale geophysics inversion using surface waves extracted from noise cross-correlation. *In 3rd Internationnal Symposium on the Effects of Surface Geology on Seismic Motion*.

Herrmann R.B. 1987. Computer programs in seismology. URL http://www.eas.slu.edu/People/RBHerrmann/ComputerPrograms.html.

Hole J., Ryberg T., Fuis G., Bleibinhaus F. and Sharma A. 2006. Structure of the San Andreas fault zone at SAFOD from a seismic refraction survey. *Geophysical Research Letters* **33**, L07312.

Kang T.-S. and Shin J.S. 2006. Surface-wave tomography from ambient seismic noise of accelerograph networks in southern Korea. *Geophysical Research Letters* **33**, L17303.

Laigle M., Hirn A., Sapin M., Lépine J., Diaz J., Gallart J. and Nicolich R. 2000. Mount Etna dense array local earthquake P and S tomography and implications for volcanic plumbing. *Journal of Geophysical Research* **105**, 21.633–21.646.

Lankar V. 1997. *Approches par tomographie sismique du Piton de la Fournaise, La Réunion*. Thèse de doctorat, Institut de Physique du Globe de Paris, France.

Larose E., Khan A., Nakamura Y. and Campillo M. 2005. Lunar subsurface investigated from correlation of seismic noise. *Geophysical Research Letters* **32**, L16201.

Larose E., Margerin L., Derode A., Tiggelen B.V., Campillo M., Shapiro N.M., Paul A., Stehly L. and Tanter M. 2006a. Correlation of random wavefields: an interdisciplinary review. *Geophysics* **71**, 4, SI11–SI21.

Larose E., Derode A., Campillo M. and Fink M. 2004. Imaging from one-bit correlation of wide-band diffuse wavefield. *Journal of Applied Physics* **95**, 8393–8399.

Larose E., Lobkis O.I. and Weaver R.L. 2006b. Passive correlation imaging of a buried scatterer. *The Journal of the Acoustical Society of America* **119**, 3549–3552.

Levshin A., Yanocskaya T.B., Lander A.V., Bukchin B.G., Barmin M.P., Ratnikova L.I. and Its E.N. 1989. *Seismic surface waves in a laterally inhomogeneous Earth*. Kluwer Academic Publishers.

Lin F., Ritzwoller M.H., Townend J., Bannister S. and Savage M. 2007. Ambiant noise Rayleigh wave tomography of New Zealand. *Geophysical Journal International* **170**, 649–666.

Lobkis O.I. and Weaver R.L. 2001. On the emergence of the Green's function in the correlations of a diffuse field. *The Journal of the Acoustical Society of America* **110**, 3011–3017.

Marchant R. and Stampfli G. 1996. Subduction of continental crust in the Western Alps. *Tectonophysics* **269**, 217–235.

Mason W.P. and Thurston R.N. 1988. *Physical Acoustics*, vol. **18**. Academic Press.

Patanè D., Barberi G., Cocina O., De Gori P. and Chiarabba C. 2006. Time-resolved seismic tomography detects magma intrusions at Mount Etna. *Science* **313**, 821–823.

Ramm A.G. 1986. *Scattering by obstacles*. Kluwer Academic Publisher.

Reed M. and Simon B. 1978. *Methods of modern mathematical physics I, II, III, IV*. Academic Press.

Ritzwoller M. and Levshin A.L. 1998. Eurasian surface wave tomography: group velocities. *Journal of Geophysical Research* **103**, 4839–4878.

Ritzwoller M.H., Shapiro N.M., Barmin M.P. and Levshin A.L. 2002. Global surface wave diffraction tomography. *Journal of Geophysical Research* **107**, B12, 2335.

Roux P. and Kuperman W.A. 2004. Extracting coherent wavefronts from acoustic ambient noise in the ocean. *The Journal of the Acoustical Society of America* **116**, 4, 1995–2003.

Roux P., Sabra K.G., Gerstoft P. and Kuperman W.A. 2005a. P-waves from cross-correlation of seismic noise. *Geophysical Research Letters* **32**, L19303.

Roux P., Sabra K.G., Kuperman W.A. and Roux A. 2005b. Ambient noise cross correlation in free space: theoretical approach. *The Journal of the Acoustical Society of America* **117**, 1, 79–84.

Sabra K.G., Gerstoft P., Roux P. and Kuperman W.A. 2005a. Surface wave tomography from microseisms in southern California. *Geophysical Research Letters* **32**, L14311.

Sabra K.G., Roux P. and Kuperman W.A. 2005b. Arrival-time structure of the time-averaged ambient noise cross-correlation function in an oceanic waveguide. *The Journal of the Acoustical Society of America* **117**, 1, 164–174.

Sabra K.G., Roux P. and Kuperman W.A. 2005c. Emergence rate of the time-domain Green's function from the ambient noise noise cross-correlation. *The Journal of the Acoustical Society of America* **118**, 6, 3524–3531.

Sánchez-Sesma F.J. and Campillo M. 2006. Retrieval of the Green function from cross correlation: the canonical elastic problem. *Bulletin of the Seismological Society of America* **96**, 1182–1191.

Sánchez-Sesma F.J., Pérez-Ruiz J., Campillo M., and Luzòn F. 2006. Elastodynamic 2-D Green function retrieval from cross-correlation: canonical inclusion problem. *Geophysical Research Letters* **33**, L13305.

Sánchez-Sesma F.J., Pérez-Ruiz J., Luzòn F., Campillo M. and Rodriguez-Castellano A. 2007. Diffuse fields in dynamic elasticity. *Wave Motion*, in press.

Shapiro N.M. and Campillo M. 2004. Emergence of broadband Rayleigh waves from correlations of the ambient seismic noise. *Geophysical Research Letters* **31**, L07614.

Shapiro N.M., Campillo M., Paul A., Singh S.K., Jongmans D. and Sànchez-Sesma F.J. 1997. Surface-wave propagation across the Mexican Volcanic Belt and the origin of the long-period seismic-wave amplification in the Valley of Mexico. *Geophysical Journal International* **128**, 151–166.

Shapiro N.M., Campillo M., Stehly L. and Ritzwoller M.H. march 2005. High-resolution surface wave tomography from ambient seismic noise. *Science* **307**, 1615–1618.

Sherburn S., White R.S. and Chadwick M. 2006. Three-dimensional tomographic imaging of the Taranaki volcanoes, New Zealand. *Geophysical Journal International* **166**, 957–969.

Snieder R. 2004. Extracting the Green's function from the correlation of coda waves: a derivation based on stationary phase. *Physical Review E* **69**, 4 Pt 2, 046610.

Stehly L., Campillo M. and Shapiro N. 2006. A study of the seismic noise from its long range correlation properties. *Journal of Geophysical Research* **111**, B10306.

Stehly L., Campillo M. and Shapiro N.M. 2007. Travel time measurements from noise correlation: stability and detection of instrumental time-shifts. *Geophysical Journal International* **171**, 223–230.

Tanaka S., Hamaguchi H., Nishimura T., Yamawaki T., Ueki S., Nakamishi H., Tsutsui T., Miyamachi H., Matsuwo N., Oikawa J., Ohminato T., Miyaoka K., Onizawa S., Mori T. and Aizawa 2002. Three-dimensional P-wave velocity structure of Iwate volcano, Japan from active seismic survey. *Geophysical Research Letters* **29**, 59–62.

Thurber C., Roecker S., Zhang H., Baher S., Ellsworth W. and Tanimoto T. 2004. Fine-scale structure of the San Andreas Fault Zone and location of the SAFOD target earthquakes (2004). *Geophysical Research Letters* **31**, L12S02.

van Tiggelen B.A. 2003. Green function retrieval and time reversal in a disordered world. *Physical Review Letter* **91**, 24, 243904.

Waldhauser F., Kissling E., Ansorge J. and Mueller S. 1998. Three-dimensional interface modelling with two-dimensional seismic data: the Alpine crust mantle boundary. *Geophysical Journal International* **135**, 264–278.

Waldhauser F., Lippitsch R., Kissling E. and Ansorge J. 2002. High-resolution teleseismic tomography of upper-mantle structure using an a priori three-dimensional crustal model. *Geophysical Journal International* **150**, 403–414.

Wapenaar K. 2004. Retrieving the elastodynamic Green's Function of an arbitrary inhomogeneous medium by cross-correlation. *Physical Review Letter* **93**, 254301.

Wapenaar K. 2006. Nonreciprocal Green's function retrieval by cross correlation. *The Journal of the Acoustical Society of America* **120**, 1, EL7–E13.

Weaver R.L. 2005. Information from seismic noise. *Science* **307**, 5715, 1568–1569.

Weaver R.L. and Lobkis O.I. 2001. Ultrasonics without a source: thermal fluctuation correlations at MHz frequencies. *Physical Review Letter* **87**, 13, 134301.

Weaver R.L. and Lobkis O.I. 2003. Elastic wave thermal fluctuations, ultrasonic waveforms by correlation of thermal phonons. *The Journal of the Acoustical Society of America* **113**, 2611–2621.

Weaver R.L. and Lobkis O.I. 2004. Diffuse fields in open systems and the emergence of the Green's function. *The Journal of the Acoustical Society of America* **116**, 5, 2731–2734.

Weaver R.L. and Lobkis O.I. 2005a. Fluctuations in diffuse field-field correlations and the emergence of the Green's function in open systems. *The Journal of the Acoustical Society of America* **117**, 3432–3439.

Weaver R.L. and Lobkis O.I. 2005b. The mean and variance of diffuse field correlations in finite bodies. *The Journal of the Acoustical Society of America* **118**, 3447–3456.

Weaver R.L. and Lobkis O.I. 2006. Diffuse fields in ultrasonics and seismology. *Geophysics* **71**, SI5–SI9.

Yang Y., Ritzwoller M.H., Levshin A.L. and Shapiro N.M. 2007. Ambient noise Rayleigh wave tomography across Europe. *Geophysical Journal International* **168**, 259–274.

Yao H., van der Hilst R.D. and de Hoop M.V. 2006. Surface-wave array tomography in SE Tibet from ambiant seismic noise and two-station analysis – I. Phase velocity maps. *Geophysical Journal International* **166**, 732–744.

Zollo A., D'Auria L., Matteis R.D., Herrero A., Virieux J. and Gasparini P. 2002. Bayesian estimation of 2-D P-velocity models from active seismic arrival time data: imaging of the shallow structure of Mt Vesuvius. *Geophysical Journal International* **151**, 566–582.

APPENDIX: DETAILED CALCULATION OF THE CROSS-CORRELATION FUNCTION (EQUATION 4)

We start from the definition of the cross-correlation function between two points A and B (equation 3) in which we express the wavefield u using the Green's function G:

$$
\begin{aligned}
&C(\tau, \vec{r}_A, \vec{r}_B) \\
&\quad = \lim_{T\to+\infty} \frac{1}{T}\int_0^T u(t, \vec{r}_A)\, \overline{u(t+\tau, \vec{r}_B)}\, dt \\
&\quad = \lim_{T\to+\infty} \frac{1}{T}\int_0^T dt \int_0^\infty ds \int_X d\vec{r}_s\; G_a(s, \vec{r}_A, \vec{r}_s)\; f(t-s, \vec{r}_s) \\
&\qquad \times \int_0^\infty ds' \int_X d\vec{r}_s{}'\; \overline{G_a(s', \vec{r}_B, \vec{r}_s{}')\; f(t+\tau-s', \vec{r}_s{}')}
\end{aligned}
$$

The large T limit can be replaced by an ensemble average, which gives the mathematical expectation denoted by $\mathbb{E}$. As f is a white noise, we have:

$$
\begin{aligned}
&\lim_{T\to+\infty} \frac{1}{T}\int_0^T f(t-s, \vec{r}_s)\; f(t+\tau-s', \vec{r}_s{}')\, dt \\
&\quad = \mathbb{E}[\, f(t-s, \vec{r}_s)\; f(t+\tau-s', \vec{r}_s{}')] \\
&\quad = \sigma^2\, \delta(\tau+s-s')\, \delta(\vec{r}_s - \vec{r}_s{}')
\end{aligned}
$$

where σ is the variance of the white noise. This property simplifies the previous equation, and we obtain:

$$
C(\tau, \vec{r}_A, \vec{r}_B) = \sigma^2 \int_0^\infty ds \int_X d\vec{r}_s\; G_a(s, \vec{r}_A, \vec{r}_s)\; \overline{G_a(s+\tau, \vec{r}_B, \vec{r}_s)}
$$

Using the expression of the Green's function (equation 2):

$$
\begin{aligned}
C(\tau, \vec{r}_A, \vec{r}_B) &= \sigma^2 \int_0^\infty ds \int_X d\vec{r}_s\; Y(s)\; Y(s+\tau)\; e^{-a s}\; e^{-a(s+\tau)} \\
&\times \left[\!\!\left[\frac{\sin s\sqrt{-L-a^2}}{\sqrt{-L-a^2}} \right]\!\!\right](\vec{r}_A, \vec{r}_s) \\
&\times \overline{\left[\!\!\left[\frac{\sin (s+\tau)\sqrt{-L-a^2}}{\sqrt{-L-a^2}} \right]\!\!\right](\vec{r}_B, \vec{r}_s)}
\end{aligned}
$$

We use two properties of the integral kernel:

$$
\overline{[\![P]\!](x, y)} = [\![\overline{P}]\!](x, y) = [\![p]\!](y, x)
$$

$$
\int_X [\![P_1]\!](x, z)\; [\![P_2]\!](z, y)\, dz = [\![P_1 \cdot P_2]\!](x, y)
$$

to obtain a new formula for the cross-correlation function:

$$
\begin{aligned}
C(\tau, \vec{r}_A, \vec{r}_B) &= \sigma^2 \int_0^\infty ds\; Y(s+\tau)\; e^{-a(2s+\tau)} \\
&\times \left[\!\!\left[\frac{\sin s\sqrt{-L-a^2}}{\sqrt{-L-a^2}}\; \frac{\sin (s+\tau)\sqrt{-L-a^2}}{\sqrt{-L-a^2}} \right]\!\!\right](\vec{r}_A, \vec{r}_B)
\end{aligned}
$$

Using $\sin\alpha \sin\beta = 1/2\,(\cos\,(\alpha-\beta) - \cos\,(\alpha+\beta))$ and computing the integral over ds, we obtain equation 4:

$$
\begin{aligned}
C(\tau, \vec{r}_A, \vec{r}_B) &= \frac{\sigma^2\, e^{-a|\tau|}}{4a} \\
&\times \left[\!\!\left[(-L)^{-1} \left(\cos\tau\sqrt{-L-a^2} + a\frac{\sin|\tau|\sqrt{-L-a^2}}{\sqrt{-L-a^2}} \right) \right]\!\!\right](\vec{r}_A, \vec{r}_B)
\end{aligned}
$$